Carbon-Encapsulated F-Doped $Li_4Ti_5O_{12}$ as a High Rate Anode Material for Li^+ Batteries

Yue Ma,[†,‡] Bo Ding,[†,‡] Ge Ji,[†] and Jim Yang Lee[†,‡,*]

[†]Department of Chemical and Biomolecular Engineering, National University of Singapore, 10 Kent Ridge Crescsent, Singapore 119260, Singapore and
[‡]NUS Graduate School for Integrative Sciences & Engineering (NGS), Centre for Life Sciences (CeLS), #05-01 28 Medical Drive, Singapore 117456, Singapore

ABSTRACT TiO_2 nanoparticles aggregated into a regular ball-in-ball morphology were synthesized by hydrothermal processing and converted to carbon-encapsulated F-doped $Li_4Ti_5O_{12}$ (LTO) composites (C-FLTO) by solid state lithiation at high temperatures. Through the careful control of the amount of carbon precursor (D(+)-glucose monohydrate) used in the process, LTO encapsulated with a continuous layer of nanoscale carbon was formed. The carbon encapsulation served a dual function: preserving the ball-in-ball morphology during the transformation from TiO_2 to LTO and decreasing the external electron transport resistance. The fluoride doping of LTO not only increased the electron conductivity of LTO through trivalent titanium (Ti^{3+}) generation, but also increased the robustness of the structure to repeated lithiation and delithiation. The best-performing composite, C-FLTO-2, therefore delivered a very satisfying performance for a LTO anode: a high charge capacity of ~158 mA h g^{-1} at the 1 C rate with negligible capacity fading for 200 cycles and an extremely high rate performance up to 140 C.

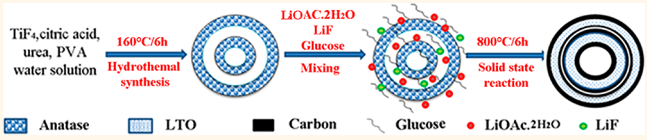

KEYWORDS: lithium titanium oxide · fluoride doping · ball-in-ball morphology · high rate · Li^+ storage

High energy density and design flexibility are the strength of lithium-ion batteries (LIBs) for large-scale applications such as electric vehicles, hybrid electric vehicles and energy storage for smart grids. However, many of the LIBs on the market today still could not provide satisfactory performance in terms of charge/discharge rates, cycle life, and some safety aspects of these applications.[1,2]

Most commercially available LIBs are formulated with graphite-based anodes for a large cell voltage. Graphite anodes are however not designed for high rate applications. Their low lithiation potential (<0.2 V *versus* Li/Li^+) causes the formation of a solid electrolyte interphase (SEI) layer on the electrode, which irreversibly consumes both electrons and Li^+.[3−6] Lithium dendrites may also form under high rate conditions to cause internal shorts. Graphite anodes also incur a volume change of 9−13% between full lithiation and full delithiation, which fatigues the graphite particles leading to a gradual loss of interparticle electrical contact and consequently cycle stability.[7−9]

Among the alternatives to the graphite anode, lithium titanium oxide ($Li_4Ti_5O_{12}$, LTO) spinel has shown very facile Li^+ storage properties highly desirable for power-oriented applications despite its limited theoretical capacity (175 mA h g^{-1}). Full lithiation of the LTO spinel leads to the occupation of the octahedral 16c sites of spinel structure and the emptying of the tetrahedral 8a sites until the final composition is $Li_7Ti_5O_{12}$. Lithiation also occurs at a relatively high potential (~1.55 V *versus* Li^+/Li) to provide a safer battery operation.[10−12] The end members of lithiation ($Li_4Ti_5O_{12}$ and $Li_7Ti_5O_{12}$) differ negligibly in lattice parameters (0.2%), and hence, LTO may be regarded as a " zero strain" material.[13−15] Although LTO in the lithiated state ($Li_7Ti_5O_{12}$) is a good conductor, LTO in the unlithiated state is electronically insulating because of the presence of Ti^{4+} with empty 3d orbitals (electronic configuration $[Ar]3d^0$) and a large band gap of ~2 eV.[16,17] Research efforts in recent years have been directed at addressing the conductivity deficiency of pristine (unlithiated) LTO through composition modulations and nanoengineering of the LTO structure.

* Address correspondence to cheleejy@nus.edu.sg.

Received for review August 18, 2013 and accepted November 20, 2013.

Published online November 20, 2013
10.1021/nn404311x

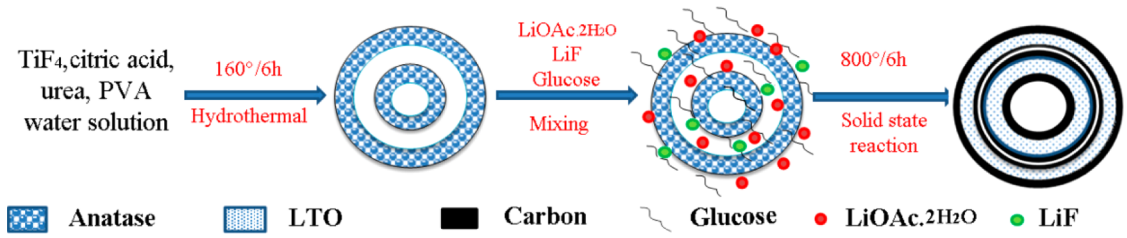

Scheme 1. Schematic of the preparation of carbon-encapsulated F-doped LTO composites (C-FLTOs).

Isovalent and aliovalent cation doping (*e.g.*, Zr^{4+}, V^{5+}, V^{4+}, Mn^{4+}, Mo^{4+}, Fe^{3+}, Al^{3+}, Ga^{3+}) at the Ti^{4+} sites have been used in previous studies to increase the electronic conductivity of LTO.[18−23] Recently, Qi *et al.* also found Br-doping at the O sites to be helpful in improving the electrochemical performance of LTO. An optimal composition of $Li_4Ti_5O_{12-x}Br_x$ (x = 0.2) was reported by the authors, improving the rate performance to a discharge capacity of 118 mA h g^{-1} at the 5 C rate and 100 mA h g^{-1} at the 10 C rate.[24,25] These improvements are noteworthy but still insufficient for power-oriented applications. Other material improvement strategies include morphology and structure modifications: using nanoscale primary particles to reduce the Li^+ diffusion length in the solid state, assembly of primary nanoparticles into a dense packing to increase structure stability, tap density and material processability; and the creation of porosity or hollow interior in the assembly to improve electrolyte percolation.[26−28] For example, Lou *et al.* recently reported the synthesis of mesoporous LTO hollow spheres. Although a relatively high rate performance of 104 mA h g^{-1} at 20 C was demonstrated, the silica templating method is rather onerous, and the large cavity of the mesoporous spheres results in a low volumetric density.[29] Zhang *et al.* prepared porous microspheres of LTO nanoparticles by a simpler template-free hydrothermal method. Li^+ transport in the material was however affected by microscale inhomogeneities, and hence, the rate performance of the electrode was lower (116 mA h g^{-1} at 10 C and 92.3 mA h g^{-1} at 20 C).[30,31] Compositing LTO with a conducting material (carbon nanotubes, graphene nanosheets, Cu, Ag, *etc.*) is another strategy to improve the charge transfer kinetics in LTO electrodes.[7,32−35]

In this project, we designed and fabricated carbon-encapsulated F-doped LTO composites (C-FLTO) by combining hydrothermal processing and a controlled solid state lithiation reaction. The composite synthesized with the optimal carbon content successfully integrated a number of original features: (1) a fluoride ion (F^-) doping technique that partially substituted [O][32e] with F in the LTO spinel, which not only induced the formation of charge compensating Ti^{3+} (serving as electron donors) to increase conductivity, but also improved the integrity of the LTO structure in discharge and charge cycling; (2) a ball-in-ball morphology that assisted electrolyte percolation; (3) nanocrystalline building blocks that shortened the solid-state Li^+ diffusion length; and (4) a nanoscale carbon encapsulation layer (∼2−4 nm) that electrically integrated the LTO primary nanoparticles with a very small capacity penalty. The carbon coating also acted as a barrier against the crystal growth of LTO nanoparticles during the high temperature treatment in the preparation. Consequently, electrochemical measurements registered a very satisfying performance: a large charge capacity (∼158 mA g^{-1}) with negligible capacity fading for 200 cycles at the 1 C rate; extremely high rate capability (109 mA g^{-1} at 30 C; 89 mA g^{-1} at 60 C; and 60 mA g^{-1} at 140 C). The postmortem analysis of the cycled electrode confirmed the contributions of fluoride doping in enhancing the electrode kinetics and increasing the robustness of the structure.

RESULTS AND DISCUSSION

The preparation of carbon-encapsulated F-doped LTO composites (C-FLTOs) is summarized in Scheme 1. TiO_2 particles with a ball-in-ball morphology (TiO_2−BB) were first synthesized and used as the Ti source in a subsequent solid state reaction. Transmission electron microscope (TEM) image of TiO_2−BB revealed diameters of 100−200 nm for the inner ball and ∼400 nm for the outer ball, which were formed from aggregates of crystalline primary nanoparticles ∼20−30 nm in size (Figure 1a and inset). A mechanism for the formation of the ball-in-ball morphology may be suggested after following the morphology evolution with time and reviewing similar hydrothermally synthesized systems in the literature.[36−38] In the early stages of the hydrothermal reaction (2 h), mesoporous spherical aggregates of hydrated TiO_2 nanoparticles (TiO_2−MS) with limited crystallinity and an average diameter of ∼300−400 nm were formed from the hydrolysis of TiF_4 (Figure S1a, Supporting Information). The presence of a cavity between the shell and the core could be attributed to diffusion-controlled dissolution and recrystallization of anatase TiO_2 in a prolonged hydrothermal reaction, which is shown as Process II in Scheme 2. The dissolution−recrystallization of TiO_2 in hydrothermal synthesis has been reasonably well understood.[36−38] In brief, the dissolution and recrystallization of hydrated TiO_2 began with the spherical surface region because of its accessibility to the

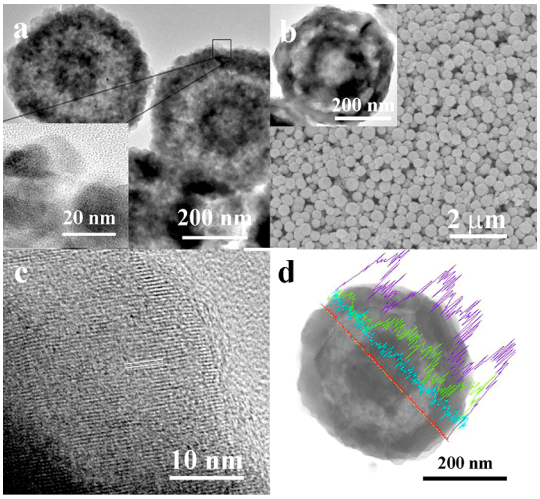

Figure 1. (a) TEM image of TiO_2—BB; (b) FESEM image of C-FLTO-2 at low magnification; (c) HRTEM image of C-FLTO-2; (d) high magnification STEM image and EDS line scan analysis of a C-FLTO-2 cross-section (purple, green, cyan, and red lines show the distributions of titanium, oxygen, carbon, and fluorine, respectively); inset (a) high magnification of TEM image of TiO_2—BB; inset (b) TEM image of a single C-FLTO-2 particle.

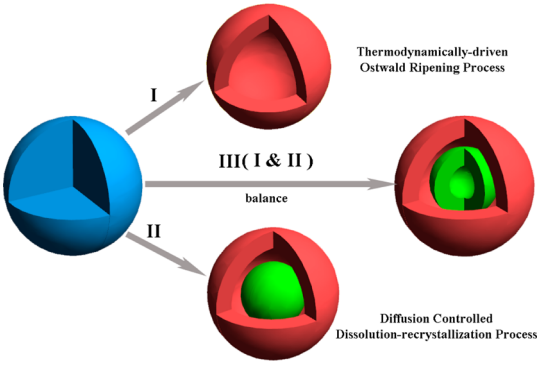

Scheme 2. Schematic showing the formation of TiO_2—BB structure. Blue represents the hydrated TiO_2 particles; red represents the outer shell of the TiO_2 structure; and green represents the internal sphere of the TiO_2 structure.

reaction medium (water). Surface charge repulsion between recrystallized anatase and the surface of undissolved hydrated TiO_2 core debilitated the interface causing microvoids to be formed between them. Solvent permeation into the microvoids further fueled the dissolution—recrystallization process, expanding the microvoids into gaps between a recrystallized external region and the pristine internal region.[38] At the same time the inner core was hollowed by Ostwald ripening (Scheme 2 (Process I)) where the metastable nanocrystallites in the core region (low in crystallinity relative to those in the outer shell) dissolved and redeposited on the outer shell. This thermodynamically driven ripening mechanism has been used to fabricate hollow anatase nanospheres in several studies and was also applicable in the current synthesis.[39,40] When the hydrothermal treatment was extended to 16 h, Ostwald ripening dominated the morphology tailoring of TiO_2; the inner sphere disappeared completely, and the product was TiO_2 hollow spheres (TiO_2—HS, TEM image in Figure S1b, Supporting Information). As shown in Figure S2 (Supporting Information), the XRD patterns of TiO_2—BB and TiO_2—HS after heat treatment at 200 °C for 12 h are characteristic of tetragonal anatase TiO_2 with the *I*41/*amd* space group (ICDD# 00-001-0562). The relatively higher peak intensity of TiO_2—HS indicates more extensive crystal growth after a longer hydrothermal treatment. The interesting TiO_2—BB morphology was only formed at an intermediate reaction time (6 h) when the diffusion-controlled dissolution—recrystallization process and the thermodynamically driven Ostwald ripening process were comparable (Scheme 2 (Process III)).

The TiO_2—BB structure, used as the LTO precursor, was uniformly mixed with $LiAc \cdot 2H_2O$, LiF and D(+)-glucose monohydrate in a predetermined ratio, and the mixture was heated at different temperatures to form various carbon/LTO composites. Among the composites, C-FLTO-2 had integrated the different structural features most optimally to provide the best electrochemical performance and as such was selected for a detailed characterization. The field emission scanning electron microscopy (FESEM) image of C-FLTO-2 (Figure 1b) shows globular particles 300—400 nm in diameter. A closer examination of a representative particle (Figure 1b inset) reveals the ball-in-ball construction with a shell thickness of 40—60 nm for both inner and outer spheres, features which were transferred from its parent titanium precursor (TiO_2—BB). The BET surface area of C-FLTO-2 as measured by multipoint BET plot (Figure S3, Supporting Information) was 18.2 $m^2\ g^{-1}$. The high resolution-TEM (HRTEM) image of C-FLTO-2 in Figure 1c shows the presence of a 3—4 nm carbon coating on the surface of the primary LTO nanoparticles. Well-defined lattice fringes with a separation of 0.48 nm were found in the HRTEM image of the carbon-coated LTO nanoparticle, corresponding well with the spacing of the (111) planes in the LTO spinel (ICDD# 00-049-0207). The scanning transmission electron microscope (STEM) image of a representative C-FLTO-2 particle is given in Figure 1d. Energy-dispersive X-ray spectroscopy (EDS) line-scan analysis (Figure 1d) across the particle diameter shows a quadrimodal distribution of Ti intensity, which further confirms the ball-in-ball morphology of C-FLTO-2.

C-FLTO-1 and C-FLTO-3, which were prepared with different carbon contents, were examined together with C-FLTO-2 to determine the effects of carbon content on electrochemical performance. This was done by mixing the TiO_2—BB precursor with different amounts of D(+)-glucose monohydrate (5 and 20 wt % of the TiO_2—BB precursor instead of the standard 10 wt %) in the preparation while keeping all other preparation parameters fixed. Thermal gravimetric

analysis (TGA) of the carbon-encapsulated LTO composites (Figure S4, Supporting Information) measured carbon contents of 2.03, 5.40, and 10.49 wt % for C-FLTO-1, C-FLTO-2, and C-FLTO-3, respectively. The TEM image in Figure S1c (Supporting Information) shows that C-FLTO-1 did not have the ball-in-ball morphology of its TiO_2—BB precursor. Instead there was severe agglomeration of the nanoparticles, suggesting that the amount of carbon coating was inadequate to maintain the ball-in-ball morphology of the precursor. On the other hand, C-FLTO-3 preserved the ball-in-ball morphology through the use of excess glucose (Figure S1d,e, Supporting Information). The thick carbon (~10 nm) may however lower the capacity of the electrode.[41,42]

The diffraction peaks in the X-ray powder diffraction (XRD) patterns of C-FLTO composites could be indexed to a cubic spinel structure from the *Fd*3*m* space group (ICDD# 00-0026-1198). (There was however some impurity due to residual anatase in the XRD pattern of C-FLTO-1 composite, probably because of insufficient carbon protection.) The mean crystallite size calculated from the (111) reflection of LTO spinel by the Scherer equation was 67 nm for C-FLTO-1, 34.8 nm for C-FLTO-2 and 30.4 nm for C-FLTO-3. This decreasing trend indicates that pyrolyzed carbon had effectively restrained the crystal growth of LTO primary nanoparticles in C-FLTO-2 and C-FLTO-3, thereby preserving the nanoscale advantage. For the composite that was prepared without the additional Li source (LiF) in the solid state reaction (C-LTO2), peaks indexable to rutile TiO_2 began to emerge in the XRD pattern (Figure 2). This is indication that without a sufficient Li supply, unreacted anatase would convert to rutile TiO_2 at the high temperature used in the anatase-to-LTO conversion. On the other hand, when LiF was substituted by an equimolar amount of $LiAc \cdot 2H_2O$ in the preparation, phase-pure LTO with the ball-in-ball morphology (C-LTO2X) and carbon encapsulation could be produced, as shown by the TEM images in Figure S1f (Supporting Information) and its inset and the XRD pattern in Figure 2. It may be concluded from these observations that a stoichiometric excess of lithium must be present in the solid state conversion from TiO_2 to LTO in order to compensate for lithium oxide volatilization at high temperature.[43,44] The effect of temperature was also investigated. The XRD patterns of composites formed by heat treatment at 700 and 600 °C (C-FLTO-700 and C-FLTO-600, respectively) indicated the coexistence of anatase TiO_2 and spinel LTO, indicating that phase transformation (lithiation of TiO_2) was incomplete at these lower temperatures. A summary of the effects of key preparation variables on the phases and the chemical composition of the LTO composites may be found in Table S1 (Supporting Information).

The presence of substitutional fluoride doping and trivalent titanium in the C-FLTO composites was

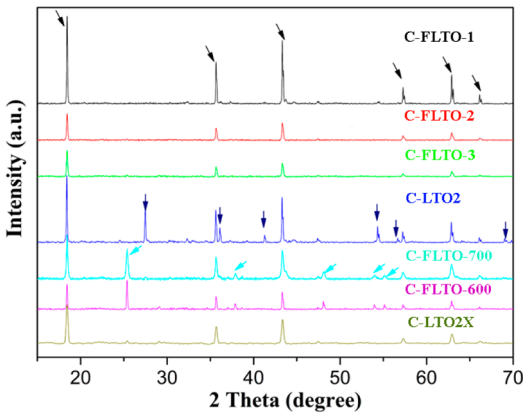

Figure 2. XRD patterns of carbon encapsulated LTO composites. (Black arrows indicate diffraction peaks indexable to LTO, blue arrows indicate diffraction peaks indexable to rutile TiO_2, and cyan arrows indicate diffraction peaks indexable to anatase TiO_2).

indicated by X-ray photoemission spectroscopy (XPS). Previous research has shown the importance of controlling the spatial distribution of anionic dopants when modifying the electronic properties of the LTO structure. The presence of anionic dopant as a surface adsorbed layer clearly would not help; neither would interstitial doping where anions in the interstice between adjacent $[Li_{1/6}Ti_{5/6}]^{16d}O_6$ octahedra are actually barriers to Li^+ diffusion.[45,46] The F 1s XPS spectrum of C-FLTO-2 in Figure 3a shows an asymmetric peak typical of the presence of F in different bonding states. The F 1s peak after curve-fitting could be deconvoluted into two peaks at binding energies of 684.8 and 686.6 eV attributable to Ti—F covalent bonds and C—F species, respectively. The presence of C—F covalent bonds was also confirmed by the slight broadening of the carbon 1s peak at 289.5 eV (Figure S5a, Supporting Information).[47,48] The lack of F 1s core-level peaks in the XPS spectrum of C-FLTO-3 (Figure S5b, Supporting Information) was due to signal attenuation caused by a thick carbon layer and was confirmed by the emergence of the Ti—F peak after argon ion-beam sputtering: The peak at ~684.8 eV increased in intensity after the carbon layer was progressively removed by 3 and 5 min of argon ion sputtering. In the high-resolution Ti 2p XPS core level XPS spectra of C-FLTO-2 and C-LTO2 in Figure 3b, the two peaks centering at ~464.7 and ~458.7 eV for C-LTO2X correspond well with the Ti $2p_{1/2}$ and Ti $2p_{3/2}$ peaks of tetravalent Ti.[49] The C-FLTO-2 spectrum, on the other hand, displayed negative shifts of these peaks indicating a change in the Ti oxidation state. The difference spectrum obtained by subtracting the normalized Ti 2p spectrum of C-LTO2X from that of C-FLTO-2 contains two positive peaks at ~463.2 and ~457.6 eV (the locations of trivalent Ti) and two valleys at 464.9 and 458.9 eV (locations of tetravalent Ti).[50,51] Taken together this suggests the creation of Ti^{3+} sites at the expense of

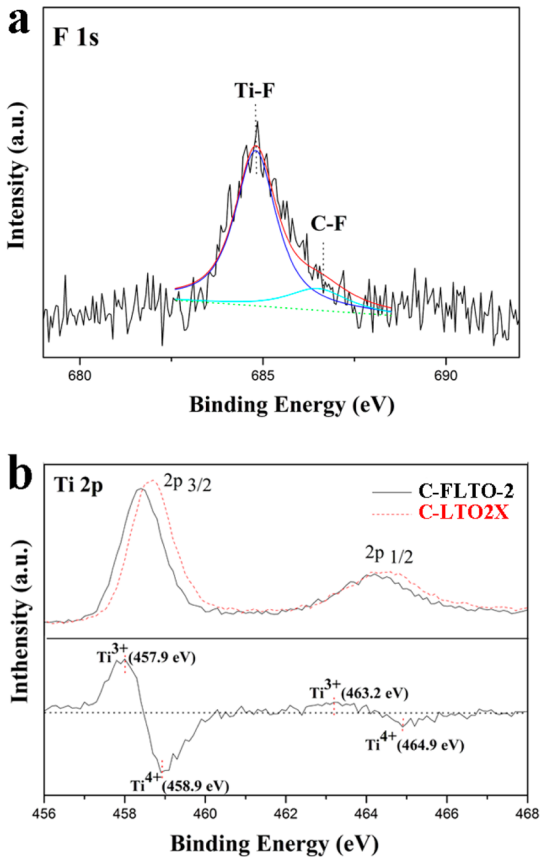

Figure 3. (a) F 1s core-level XPS spectrum of C-FLTO-2. (b) Superposition of the normalized Ti 2p core spectra of C-FLTO-2 and C-LTO-2X and the difference in their spectral features.

Ti^{4+} in C-FLTO-2. Quantification of the XPS spectrum of C-FLTO-2 with the Vision software provided by the manufacturer (Kratos) yielded a F to O atomic ratio of 1.45:100, based on which the molecular formula $Li4Ti_5O_{12-x}F_x$ (x = 0.174) may be written. Hence 17.4 atom % of the fluorine in LiF was transferred to the LTO lattice by the solid state reaction. Correspondingly, it was calculated that 3.48% of the total Ti atoms were in the trivalent state to compensate for the charge imbalance when F^- substituted for lattice O^{2-}. This small amount of Ti^{3+} could however improve the electron conduction in LTO significantly by mixed valence electron hopping. The electrode kinetics could be enhanced as a result.[52]

The integration of crystalline nanoparticles, a ball-in-ball morphology, fluoride doping as well as a nanocarbon conducting network should lead to improvements in mixed conducting properties and therefore the overall electrochemical reversibility for Li^+ storage. The electrochemical performance of carbon-coated F-LTO composites for reversible Li^+ storage in Swagelok type Li half cells is shown in Figure 4. At the standard discharge−charge rate of 1 C, the cyclability of C-FLTO-1 as shown in Figure 4a is rather unsatisfactory. While the electrode delivered a first charge capacity of 151 mA h g^{-1}, it decreased to 91 mA h g^{-1} after 100 cycles of discharge−charge. This disappointing cycling performance could categorically be attributed to the large primary nanoparticle size and inadequate carbon coating. C-FLTO-2 exhibited a higher capacity with substantially lower capacity fading in repeated cycling: the first cycle discharge capacity was as high as ~172 mA h g^{-1} (the capacity was normalized by the mass of the electrode), which was higher than the maximum capacity of the electrode based on LTO alone (theoretical capacity of LTO × mass fraction of composite in the electrode × mass fraction of LTO in the composite = 175 × 0.85 × (1−5.4%) = 140 mA h g^{-1}). On the basis of density functional theory calculations and experimental results from previous studies, the higher-than-theoretical capacity could be explained by the possible occupation of the 8a sites of nanoscale LTO by Li^+ when the storage limit at the 16c sites of the spinel structure was exceeded.[27,53] The co-occupation of 8a and 16c sites in the surface region is expected to be more significant in nanoscale materials where the specific surface area is larger, resulting in storage properties different from those of the bulk.[54−56] A capacity of 166 mA h g^{-1} was returned in the reverse charge process. Remarkable cycle stability was demonstrated from the second cycle onward: the C-FLTO-2 electrode could still provide a high charge capacity of 159 mA h g^{-1} (95.8% of the first cycle) after 200 cycles of discharge and recharge with high Coulombic efficiency close to 100%. Two complementary factors clearly contributed to this considerable cyclability improvement (relative to C-FLTO-1): (1) The complete encapsulation of the LTO hollow structure with a pervasive network of carbon from the pyrolysis of D(+)-glucose monohydrate. (2) The pyrolyzed carbon matrix also isolated the nanoparticles so that the conversion of anatase TiO_2 to LTO could be localized to individual nanoparticles. This not only preserved the unique architecture of the TiO_2−BB precursor in C-FLTO-2, but also effectively inhibited the crystal growth of LTO nanoparticles during high temperature treatment. These structural factors were apparently near-optimal in C-FLTO-2 resulting in significant improvement of the electrode kinetics. The electrode based on C-FLTO-3, however, only delivered a charge capacity of 131 mA h g^{-1} at the end of 100 cycles. The smaller capacity could be attributed to the decrease in the proportion of electrochemically active component (LTO) in the composite relative to C-FLTO-2. Hence the carbon content has to be optimized to balance the concurrent needs for high active material content and electrical conductivity. Significant deviations from optimality would introduce compensatory effects between these factors. The cycling performance of C-LTO2X was also tested to shed light on the effect of fluoride doping. As shown in Figure 4a, the cycle stability of the fluorine-free C-LTO2X was

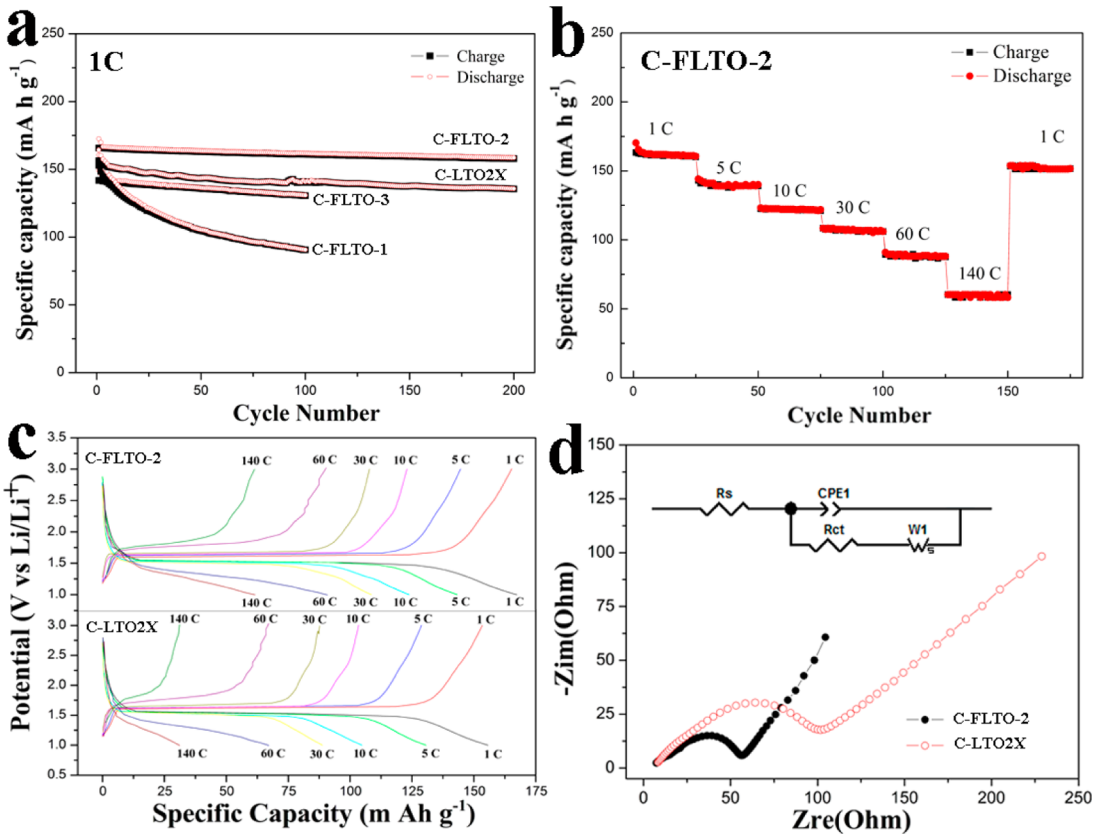

Figure 4. (a) Cyclability of C-FLTO-1, C-FLTO-2, C-FLTO-3, and C-LTO2X at the 1 C rate. (b) Cycle stability of C-FLTO-2 at different C rates. (c) The discharge−charge curves of C-FLTO-2 and C-LTO2X electrodes at different C rates. (d) Nyquist plots of delithiated C-FLTO-2 and C-LTO2X electrodes after 50 cycles of discharge and recharge at 1 C. The frequency range used for the measurements was 100 kHz−0.1 Hz.

inferior to C-FLTO-2, and the charge capacity after 200 cycles was also lower (136 mA h g^{-1}). Hence fluoride doping not also increased electrode kinetics to greater capacities, it also contributed to greater cycle stability because of a more robust structure, as will be shown below.

The discharge−charge capacities of C-FLTO-2 were also measured at different C rates (Figure 4b). A total of 175 cycles were used, and the results indicate remarkable resilience in rate performance and capacity retention. The electrode was initially cycled at 1 C where charge capacity was 162 mA h g^{-1} in the first 25 cycles. The rate was then increased stepwise to 5, 10, 30, 60, and 140 C in succession, and capacities of 144, 123, 108, 91, and 60 mA h g^{-1} stable for 25 discharge−charge cycles at each of these rates were obtained. When the C-rate was finally returned to its initial value of 1 C after a total of 150 cycles, a charge capacity of 154 mA h g^{-1} was still available and was at this value for the next 25 cycles with negligible losses. Such demonstration of excellent rate capability makes C-FLTO-2 particularly suitable for high power LIBs.

Figure 4c shows the voltage-capacity profiles of C-FLTO-2 (F-containing) and C-LTO2X (non-F-containing) electrodes cycled at different C rates in the 1.0−3.0 V voltage window. (The plotted profiles were taken from the fifth cycle of each C rate.) The decrease in capacity with the increase in C-rate is an innate material response, but the difference between the charge capacities of two electrodes was magnified with the increase in the C-rate shown in Figure S6 (Supporting Information) (*e.g.*, 10 mA h g^{-1} at 1 C, 19 mA h g^{-1} at 30 C and 29 mA h g^{-1} at 140 C). This is indication that fluoride doping is particularly effective for improving the performance of LTO at high current densities.

The increase in the rate capability of LTO by fluoride doping had to be caused by some enhancements of the electrode kinetics which could be shown more directly by electrochemical impedance spectroscopy (EIS) measurements. The C-FLTO-2 and C-LTO2X electrodes were analyzed by EIS at open-circuit voltages in their native states (before cycling) and after 50 cycles of discharge and charge. The resulting Nyquist plots (Figure 4d and Figure S7, Supporting Information) show the common features of a purely resistive response at the high frequency end, a semicircle in the high-to-middle frequency region, and an inclined straight line in the low frequency region.[57] The semicircular arc of the C-FLTO-2 electrode before cycling was much smaller compared with the C-LTO2X electrode as shown in Figure S7 (Supporting Information).[50,58] EIS measurements taken after 50 cycles

displayed the same trend (Figure 4d) of a smaller arc in the Nyquist plot of C-FLTO-2. The smaller semicircular arc is an indication of an overall smaller charge transfer resistance or, equivalently, a more facile charge transfer process at the electrode/electrolyte interface after fluoride doping. The inclined line in the low-frequency region may be categorically attributed to the Warburg impedance (Z_w) associated with Li^+ diffusion in the bulk of the material. The Warburg-like response of C-FLTO-2 electrode (Figure 4d) exhibited a larger slope, which may be used to suggest a higher Li^+ mobility in the solid compared with C-LTO2X.[58−60] Furthermore, an indicative "exchange current density" could also be calculated from the equation of $i^0 = RT/nFR_{ct}$. In this way the fluoride doped C-FLTO-2 electrode after 50 cycles had nearly doubled the charge-transfer kinetics of F-free C-LTO2X electrode (i^0 = 0.54 *versus* 0.29 mA cm^{-2}).

The TEM examination of C-FLTO-2 postmortem indicated robustness of the structure, with the ball-in-ball morphology still intact after 50 cycles at the 1 C rate (Figure S8a, Supporting Information). On the contrary the postmortem analysis of C-LTO2X showed densely agglomerated spheres and the loss of the internal cavity (Figure S8b, Supporting Information). Hence carbon coating alone was inadequate to stabilize the hollow host structure. It is hypothesized that the strong structural integrity of C-FLTO-2 composite could be attributed to the following fluorine substitution effects: (1) the presence of a small degree of strong Ti−F bonding stabilized the lattice structure;[47] (2) fluoride doping may have protected the LTO structure from corrosion by acidic species from the hydrolysis or decomposition of $LiPF_6$, such as HF, PF_5 and POF_3 in the electrolyte.[61,62]

CONCLUSION

In conclusion, we have improved the current performance of LTO for reversible Li^+ storage by promoting the complementarity of factors important to electron and Li^+ conduction in an integrated materials design: fluoride doping of the LTO lattice to increase electronic conductivity through mixed valency (Ti^{3+}/Ti^{4+}) creation, hollow nanostructures to facilitate electrolyte percolation, nanoscale primary nanoparticles to shorten the Li^+ diffusion length in the solid state, and a pervasive nanocarbon coating to decrease the external (interparticle) electrical resistance. The balance of these effects was most optimal in the C-FLTO-2 composite, where high charge capacity (158 mA g^{-1}) and good cyclability at the standard rate (1 C) and extreme high-rate capability up to 140 C (108 mA h g^{-1} at 30 C, 91 mA h g^{-1} at 60 C and 60 mA h g^{-1}at 140 C) were simultaneously possible. These findings indicate fluoride doping as an effective low cost alternative to aliovalent cationic doping of LTO. They also emphasize that multiple modification strategies (*e.g.*, nanoscale and morphology engineering, composition modifications, mixed valence conduction, and *etc.*) may be applied to improve a material performance, but they must be in the right balance to achieve the desired outcome.

METHODS

Materials. All chemicals were used as received without further purification. These chemicals were titanium(IV) fluoride (TiF_4, 99%), urea (H_2NCONH_2, 98%), citric acid ($HOC(COOH)(CH_2COOH)_2$, 99%), lithium acetate dihydrate ($LiAc\cdot 2H_2O$, 99.5%), lithium fluoride (LiF, 99.98%), metallic Li foil (99.9%), polyvinylidene difluoride (PVDF) and *N*-methylpyrrolidone (NMP) from Sigma-Aldrich; polyvinyl alcohol (MW = 115000) from BDH Laboratory Supplies; D(+)-glucose monohydrate ($C_6H_{12}O_6.H_2O$) from Merck KGaA; Super P conductive carbon black (Super C65) from Timcal, Ltd., (provided free); and a formulated battery electrolyte from Hohsen Corp (1 M $LiPF_6$ solution in a 1:1:1 (v/v) mixture of ethylene carbonate (EC), diethyl carbonate (DEC) and dimethyl carbonate (DMC)). Ultrapure water (Millipore) with resistivity higher than 18.2 MΩ cm was the solvent for hydrothermal processing.

Synthesis of TiO_2 Structures with Tailorable Morphologies. TiO_2 with tailorable morphologies were prepared by a hydrothermal reaction, which was run for different lengths of time. In a typical synthesis, 200 mg of TiF_4 was dissolved in 30 mL of water at room temperature. After 10 min of magnetic stirring, 200 mg of PVA, 400 mg of urea and 100 mg of citric acid were added in sequence. The homogenized solution was transferred to a 50 mL Teflon-lined stainless steel autoclave, sealed, and heated in an electric oven at 160 °C for 2 h. The solid product from the hydrothermal reaction was recovered by centrifugation, washed with ethanol and water in turns, and vacuum-dried at 100 °C for 6 h. The product obtained as such was mesoporous spherical aggregates of hydrated TiO_2 nanoparticles and was designated as TiO_2−MS. When the hydrothermal reaction was prolonged to 6 and 18 h while keeping all other preparation conditions fixed, ball-in-ball structures (TiO_2−BB) and hollow spheres (TiO_2−HS) were produced respectively.

Synthesis of Carbon-Encapsulated LTO Composites. 200 mg of TiO_2−BB were mixed with $LiAc\cdot 2H_2O$ in a 5:4 mol ratio (the LTO stoichiometry). The mixture was ground in an agate mortar and dispersed in 10 mL of ethanol under magnetic stirring to form Solution A. A calculated amount of LiF to provide Li:Ti = 1:1 in the final product was added to Solution A. Separately D(+)-glucose monohydrate in an amount corresponding to 5, 10, and 20 wt % of TiO_2, respectively, was dissolved in 5 mL of ethanol to make up Solution B. Solution B was added dropwise to Solution A with stirring, followed by slow evaporation at 80 °C into a consistent slurry. The slurry was then heated in nitrogen at 800 °C for 6 h. The products formed as such with different carbon contents were designated as C-FLTO-1, C-FLTO-2 and C-FLTO-3, respectively. A composite corresponding to C-FLTO-2 but without any LiF in the preparation was also synthesized, and identified as C-LTO2. Two more composites were also prepared by lowering the heat treatment temperature to 700 or 600 °C, and they were named as C-FLTO-700 and C-FLTO-600, respectively. When $LiAc\cdot 2H_2O$ was used in lieu of LiF in Solution A while keeping other parameters the same as those in the preparation of C-FLTO-2, the product so obtained was designated as C-LTO2X.

Specimens for postmortem analysis were prepared as follows: the composite electrodes were cycled at 1 C for 50 cycles and then rested for 24 h. The anode materials were then separated from the current collector in a glovebox followed by washing with NMP and vacuum drying at 100 °C for 12 h.

Materials Characterization. A 10 kV JEOL JSM-6700F scanning electron microscope was used for field emission scanning electron microscopy (FESEM). *In situ* energy-dispersive X-ray (EDX) analysis was performed during the FESEM session with a Horiba EMAX attachment analyzer. Transmission electron microscope (TEM), high resolution-TEM (HR-TEM), and scanning transmission electron microscope (STEM) images were taken on a JEOL JEM-2010F operating at 200 kV. STEM/EDX data was collected with an Oxford EDXS system and processed by the Inca software. X-ray powder diffraction patterns (XRD) of the composites were recorded on a Bruker D8 ADVANCE Diffractometer using Cu Kα radiation. X-ray photoemission spectroscopy (XPS) was performed on a KRATOS AXIS Hsi spectrometer using Al K radiation. Thermal gravimetric analysis (TGA) in air was performed on a Shimadzu-DTG-60H where temperature was ramped from 40 to 700 °C at 10 °C/min.

Electrochemical Measurements. The electrochemical properties of the composites for reversible Li^+ storage were evaluated by galvanostatic discharging and charging. The working electrode was fabricated by mixing 85 wt % composite, 5 wt % conductive additive (Super-P carbon black), and 10 wt % polyvinylidene difluoride (PVDF) binder in *N*-methylpyrrolidone (NMP) into a homogeneous slurry. The slurry was applied to a copper foil current collector and vacuum-dried at 120 °C for 12 h. The mass loadings of the as-fabricated electrodes were around 2−3 mg cm^{-2}. A lithium metal foil was used as the counter electrode and the electrolyte was 1 M $LiPF_6$ solution in a 1:1:1 (v/v) mixture of ethylene carbonate (EC), diethyl carbonate (DEC) and dimethyl carbonate (DMC). Battery cell assembly was carried out in a recirculating Ar glovebox where the moisture and oxygen contents were below 1 ppm each. The test cells were discharged (Li^+ insertion) and charged (Li^+ extraction) galvanostatically at room temperature in the 1−3 V voltage window at different C rates (1 C = 175 mA h g^{-1}) on a Neware BTS-610 battery tester. A μAutolab Type III potententiostat/galvanostat with FRA2 frequency analyzer and Nova 1.5 software were used for electrochemical impedance spectroscopy (EIS). Impedance was measured for electrodes in the fully delithiated state in the frequency range of 100 kHz to 0.1 Hz with a small perturbation of ±10 mV.

Conflict of Interest: The authors declare no competing financial interest.

Acknowledgment. Y. Ma gratefully acknowledges the financial support from the National University of Singapore Graduate School for Integrative Science and Engineering (NGS) and free Super-P samples from Timcal, Ltd., for this project.

Supporting Information Available: Microscope images of other as-fabricated TiO_2 and C/LTO compounds, XRD patterns of the hydrothermal products TiO_2−BB and TiO_2−HS, multipoint BET plot and nitrogen sorption isotherms of C-FLTO-2 composite, TGA curves of C/LTO composites, additional XPS spectra of C-FLTO-2, Nyquist plots of electrodes before cycling, postmortem TEM images of electrodes after cycling, table of key preparation parameters and properties for C/LTO composites. This material is available free of charge *via* the Internet at http://pubs.acs.org.

REFERENCES AND NOTES

1. Armand, M.; Tarascon, J. M. Building Better Batteries. *Nature* **2008**, *451*, 652–657.
2. Kang, B.; Ceder, G. Battery Materials for Ultrafast Charging and Discharging. *Nature* **2009**, *458*, 190–193.
3. Tarascon, J. M.; Armand, M. Issues and Challenges Facing Rechargeable Lithium Batteries. *Nature* **2001**, *414*, 359–367.
4. Sun, Y.-K.; Myung, S.-T.; Park, B.-C.; Prakash, J.; Belharouak, I.; Amine, K. High-Energy Cathode Material for Long-Life and Safe Lithium Batteries. *Nat. Mater.* **2009**, *8*, 320–324.
5. Yang, S.; Feng, X.; Müllen, K. Sandwich-Like, Graphene-Based Titania Nanosheets with High Surface Area for Fast Lithium Storage. *Adv. Mater.* **2011**, *23*, 3575–3579.
6. Goodenough, J. B.; Kim, Y. Challenges for Rechargeable Li Batteries. *Chem. Mater.* **2010**, *22*, 587–603.
7. Kang, E.; Jung, Y. S.; Kim, G.-H.; Chun, J.; Wiesner, U.; Dillon, A. C.; Kim, J. K.; Lee, J. Highly Improved Rate Capability for a Lithium-Ion Battery Nano-Li4Ti5O12 Negative Electrode *via* Carbon-Coated Mesoporous Uniform Pores with a Simple Self-Assembly Method. *Adv. Funct. Mater.* **2011**, *21*, 4349–4357.
8. Koyama, Y.; Chin, T. E.; Rhyner, U.; Holman, R. K.; Hall, S. R.; Chiang, Y. M. Harnessing the Actuation Potential of Solid-State Intercalation Compounds. *Adv. Funct. Mater.* **2006**, *16*, 492–498.
9. Zhao, L.; Hu, Y.-S.; Li, H.; Wang, Z.; Chen, L. Porous Li4Ti5O12 Coated with N-Doped Carbon from Ionic Liquids for Li-Ion Batteries. *Adv. Mater.* **2011**, *23*, 1385–1388.
10. Jansen, A. N.; Kahaian, A. J.; Kepler, K. D.; Nelson, P. A.; Amine, K.; Dees, D. W.; Vissers, D. R.; Thackeray, M. M. Development of High-Power Lithium-Ion Battery. *J. Power Sources* **1999**, *81−82*, 902–905.
11. Ferg, E.; Gummow, R. J.; de Kock, A.; Thackeray, M. M. Spinel Anodes for Lithium-Ion Batteries. *J. Electrochem. Soc.* **1994**, *141*, L147–L150.
12. Lu, X.; Zhao, L.; He, X.; Xiao, R.; Gu, L.; Hu, Y.-S.; Li, H.; Wang, Z.; Duan, X.; Chen, L.; Maier, J.; *et al.* Lithium Storage in Li4Ti5O12 Spinel: The Full Static Picture from Electron Microscopy. *Adv. Mater.* **2012**, *24*, 3233–3238.
13. Ohzuku, T.; Ueda, A.; Yamamoto, N. Zero-Strain Insertion Material of Li[Li1/3Ti5/3]O4 for Rechargeable Lithium Cells. *J. Electrochem. Soc.* **1995**, *142*, 1431–1435.
14. Scharner, S.; Weppner, W.; Schmid-Beurmann, P. Evidence of Two-Phase Formation upon Lithium Insertion into the Li1.33Ti1.67O4 Spinel. *J. Electrochem. Soc.* **1999**, *146*, 857–861.
15. Zaghib, K.; Simoneau, M.; Armand, M.; Gauthier, M. Electrochemical Study of Li4Ti5O12 as Negative Electrode for Li-Ion Polymer Rechargeable Batteries. *J. Power Sources* **1999**, *81−82*, 300–305.
16. Park, K.-S.; Benayad, A.; Kang, D.-J.; Doo, S.-G. Nitridation-Driven Conductive Li4Ti5O12 for Lithium Ion Batteries. *J. Am. Chem. Soc.* **2008**, *130*, 14930–14931.
17. Ouyang, C. Y.; Zhong, Z. Y.; Lei, M. S. *Ab Initio* Studies of Structural and Electronic Properties of Li4Ti5O12 Spinel. *Electrochem. Commun.* **2007**, *9*, 1107–1112.
18. Kubiak, P.; Garcia, A.; Womes, M.; Aldon, L.; Olivier-Fourcade, J.; Lippens, P.-E.; Jumas, J.-C. Phase Transition in the Spinel Li4Ti5O12 Induced by Lithium Insertion: Influence of the Substitutions Ti/V, Ti/Mn, Ti/Fe. *J. Power Sources* **2003**, *119−121*, 626–630.
19. Mukai, K.; Ariyoshi, K.; Ohzuku, T. Comparative Study of Li[CrTi]O4, Li[Li1/3Ti5/3]O4 and Li1/2Fe1/2[Li1/2Fe1/2Ti]O4 in Non-Aqueous Lithium Cells. *J. Power Sources* **2005**, *146*, 213–216.
20. Yi, T.-F.; Xie, Y.; Jiang, L.-J.; Shu, J.; Yue, C.-B.; Zhou, A.-N.; Ye, M.-F. Advanced Electrochemical Properties of Mo-Doped Li4Ti5O12 Anode Material for Power Lithium Ion Battery. *RSC. Adv.* **2012**, *2*, 3541–3547.
21. Zhao, H.; Li, Y.; Zhu, Z.; Lin, J.; Tian, Z.; Wang, R. Structural and Electrochemical Characteristics of Li4−xAlxTi5O12 as Anode Material for Lithium-Ion Batteries. *Electrochim. Acta* **2008**, *53*, 7079–7083.
22. Jeong, E. D.; Han, H. J.; Jung, O. S.; Ha, M. G.; Doh, C. H.; Hwang, M. J.; Yang, H.-S.; Hong, K. S. Characterizations and Electrochemical Performance of Pure and Metal-Doped Li4Ti5O12 for Anode Materials of Lithium-Ion Batteries. *Mater. Res. Bull.* **2012**, *47*, 2847–2850.
23. Yi, T.-F.; Jiang, L.-J.; Shu, J.; Yue, C.-B.; Zhu, R.-S.; Qiao, H.-B. Recent Development and Application of Li4Ti5O12 as Anode Material of Lithium Ion Battery. *J. Phys. Chem. Solids* **2010**, *71*, 1236–1242.
24. Qi, Y.; Huang, Y.; Jia, D.; Bao, S.-J.; Guo, Z. P. Preparation and Characterization of Novel Spinel Li4Ti5O12−xBrx Anode Materials. *Electrochim. Acta* **2009**, *54*, 4772–4776.
25. Du, G.; Sharma, N.; Peterson, V. K.; Kimpton, J. A.; Jia, D.; Guo, Z. Br-Doped Li4Ti5O12 and Composite TiO2 Anodes for Li-Ion Batteries: Synchrotron X-Ray and *In-Situ* Neutron Diffraction Studies. *Adv. Funct. Mater.* **2011**, *21*, 3990–3997.

26. Prakash, A. S.; Manikandan, P.; Ramesha, K.; Sathiya, M.; Tarascon, J. M.; Shukla, A. K. Solution-Combustion Synthesized Nanocrystalline Li4Ti5O12 As High-Rate Performance Li-Ion Battery Anode. *Chem. Mater.* **2010**, *22*, 2857–2863.
27. Borghols, W. J. H.; Wagemaker, M.; Lafont, U.; Kelder, E. M.; Mulder, F. M. Size Effects in the Li4+xTi5O12 Spinel. *J. Am. Chem. Soc.* **2009**, *131*, 17786–17792.
28. Poizot, P.; Laruelle, S.; Grugeon, S.; Dupont, L.; Tarascon, J. M. Nano-Sized Transition-Metal Oxides as Negative-Electrode Materials for Lithium-Ion Batteries. *Nature* **2000**, *407*, 496–499.
29. Yu, L.; Wu, H. B.; Lou, X. W. Mesoporous Li4Ti5O12 Hollow Spheres with Enhanced Lithium Storage Capability. *Adv. Mater.* **2013**, *25*, 2296–2300.
30. Cheng, L.; Yan, J.; Zhu, G.-N.; Luo, J.-Y.; Wang, C.-X.; Xia, Y.-Y. General Synthesis of Carbon-Coated Nanostructure Li4Ti5O12 as a High Rate Electrode Material for Li-Ion Intercalation. *J. Mater. Chem.* **2010**, *20*, 595–602.
31. Harris, S. J.; Lu, P. Effects of Inhomogeneities—Nanoscale to Mesoscale—on the Durability of Li-Ion Batteries. *J. Phys. Chem. C* **2013**, *117*, 6481–6492.
32. Zhang, B.; Liu, Y.; Huang, Z.; Oh, S.; Yu, Y.; Mai, Y.-W.; Kim, J.-K. Urchin-Like Li4Ti5O12-Carbon Nanofiber Composites for High Rate Performance Anodes in Li-Ion Batteries. *J. Mater. Chem.* **2012**, *22*, 12133–12140.
33. Shen, L.; Yuan, C.; Luo, H.; Zhang, X.; Yang, S.; Lu, X. *In Situ* Synthesis of High-Loading Li4Ti5O12-Graphene Hybrid Nanostructures for High Rate Lithium Ion Batteries. *Nanoscale* **2011**, *3*, 572–574.
34. Huang, S.; Wen, Z.; Lin, B.; Han, J.; Xu, X. The High-Rate Performance of the Newly Designed Li4Ti5O12/Cu Composite Anode for Lithium Ion Batteries. *J. Alloys Compd.* **2008**, *457*, 400–403.
35. Huang, S.; Wen, Z.; Zhang, J.; Yang, X. Improving the Electrochemical Performance of Li4Ti5O12/Ag Composite by An Electroless Deposition Method. *Electrochim. Acta* **2007**, *52*, 3704–3708.
36. Ma, Y.; Ji, G.; Ding, B.; Lee, J. Y. Facile Solvothermal Synthesis of Anatase TiO2 Microspheres with Adjustable Mesoporosity for the Reversible Storage of Lithium Ions. *J. Mater. Chem.* **2012**, *22*, 24380–24385.
37. Pan, J. H.; Zhang, X.; Du, A. J.; Sun, D. D.; Leckie, J. O. Self-Etching Reconstruction of Hierarchically Mesoporous F-TiO2 Hollow Microspherical Photocatalyst for Concurrent Membrane Water Purifications. *J. Am. Chem. Soc.* **2008**, *130*, 11256–11257.
38. Pan, J. H.; Han, G.; Zhou, R.; Zhao, X. S. Hierarchical N-doped TiO2 Hollow Microspheres Consisting of Nanothorns with Exposed Anatase {101} Facets. *Chem. Commun.* **2011**, *47*, 6942–6944.
39. Zeng, H. C. Synthesis and Self-assembly of Complex Hollow Materials. *J. Mater. Chem.* **2011**, *21*, 7511–7526.
40. Yang, H. G.; Zeng, H. C. Preparation of Hollow Anatase TiO2 Nanospheres *via* Ostwald Ripening. *J. Phys. Chem. B* **2004**, *108*, 3492–3495.
41. Wagemaker, M.; van Eck, E. R. H.; Kentgens, A. P. M.; Mulder, F. M. Li-Ion Diffusion in the Equilibrium Nanomorphology of Spinel Li4+xTi5O12. *J. Phys. Chem. B* **2008**, *113*, 224–230.
42. Chen, Z.; Belharouak, I.; Sun, Y. K.; Amine, K. Titanium-Based Anode Materials for Safe Lithium-Ion Batteries. *Adv. Funct. Mater.* **2013**, *23*, 959–969.
43. Jiang, C.; Zhou, Y.; Honma, I.; Kudo, T.; Zhou, H. Preparation and Rate Capability of Li4Ti5O12 Hollow-Sphere Anode Material. *J. Power Sources* **2007**, *166*, 514–518.
44. Wang, Y.-Q.; Gu, L.; Guo, Y.-G.; Li, H.; He, X.-Q.; Tsukimoto, S.; Ikuhara, Y.; Wan, L.-J. Rutile-TiO2 Nanocoating for a High-Rate Li4Ti5O12 Anode of a Lithium-Ion Battery. *J. Am. Chem. Soc.* **2012**, *134*, 7874–7879.
45. Jiao, W.; Li, N.; Wang, L.; Wen, L.; Li, F.; Liu, G.; Cheng, H.-M. High-Rate Lithium Storage of Anatase TiO2 Crystals Doped with Both Nitrogen and Sulfur. *Chem. Commun.* **2013**, *49*, 3461–3463.
46. Liu, G.; Wang, L.; Sun, C.; Yan, X.; Wang, X.; Chen, Z.; Smith, S. C.; Cheng, H.-M.; Lu, G. Q. Band-to-Band Visible-Light Photon Excitation and Photoactivity Induced by Homogeneous Nitrogen Doping in Layered Titanates. *Chem. Mater.* **2009**, *21*, 1266–1274.
47. Woo, S.-U.; Park, B.-C.; Yoon, C. S.; Myung, S.-T.; Prakash, J.; Sun, Y.-K. Improvement of Electrochemical Performances of Li[Ni0.8Co0.1Mn0.1]O2 Cathode Materials by Fluorine Substitution. *J. Electrochem. Soc.* **2007**, *154*, A649–A655.
48. Seo, H.; Baker, L. R.; Hervier, A.; Kim, J.; Whitten, J. L.; Somorjai, G. A. Generation of Highly n-Type Titanium Oxide Using Plasma Fluorine Insertion. *Nano Lett.* **2010**, *11*, 751–756.
49. Chen, X.; Liu, L.; Yu, P. Y.; Mao, S. S. Increasing Solar Absorption for Photocatalysis with Black Hydrogenated Titanium Dioxide Nanocrystals. *Science* **2011**, *331*, 746–750.
50. Shen, L.; Uchaker, E.; Zhang, X.; Cao, G. Hydrogenated Li4Ti5O12 Nanowire Arrays for High Rate Lithium Ion Batteries. *Adv. Mater.* **2012**, *24*, 6502–6506.
51. Liu, Y.; Szeifert, J. M.; Feckl, J. M.; Mandlmeier, B.; Rathousky, J.; Hayden, O.; Fattakhova-Rohlfing, D.; Bein, T. Niobium-Doped Titania Nanoparticles: Synthesis and Assembly into Mesoporous Films and Electrical Conductivity. *ACS Nano* **2010**, *4*, 5373–5381.
52. Kim, C.; Norberg, N. S.; Alexander, C. T.; Kostecki, R.; Cabana, J. Mechanism of Phase Propagation During Lithiation in Carbon-Free Li4Ti5O12 Battery Electrodes. *Adv. Funct. Mater.* **2013**, *23*, 1214–1222.
53. Ganapathy, S.; Wagemaker, M. Nanosize Storage Properties in Spinel Li4Ti5O12 Explained by Anisotropic Surface Lithium Insertion. *ACS Nano* **2012**, *6*, 8702–8712.
54. Zhong, Z.; Ouyang, C.; Shi, S.; Lei, M. *Ab Initio* Studies on Li4+xTi5O12 Compounds as Anode Materials for Lithium-Ion Batteries. *Chem. Phys. Chem.* **2008**, *9*, 2104–2108.
55. Hirayama, M.; Kim, K.; Toujigamori, T.; Cho, W.; Kanno, R. Epitaxial Growth and Electrochemical Properties of Li4Ti5O12 Thin-Film Lithium Battery Anodes. *Dalton Trans.* **2011**, *40*, 2882–2887.
56. Hariharan, S.; Ramar, V.; Balaya, P. Influence of Nanosize and Thermodynamics on Lithium Storage in Insertion and Conversion Reactions. *Energy Harvesting and Storage: Materials, Devices, and Applications III*; SPIE Press: Bellingham, WA, 2012; pp 837703−837703.
57. Shenouda, A. Y.; Murali, K. R. Electrochemical Properties of Doped Lithium Titanate Compounds and Their Performance in Lithium Rechargeable Batteries. *J. Power Sources* **2008**, *176*, 332–339.
58. Nimon, E. S.; Churikov, A. V. Electrochemical Behaviour of Li-Sn, Li-Cd and Li-Sn-Cd Alloys in Propylene Carbonate Solution. *Electrochim. Acta* **1996**, *41*, 1455–1464.
59. Yang, J.; Martin, D. C. Microporous Conducting Polymers on Neural Microelectrode Arrays: II. Physical Characterization. *Sens. Actuators, A* **2004**, *113*, 204–211.
60. Ma, Y.; Zhang, C.; Ji, G.; Lee, J. Y. Nitrogen-Doped Carbon-Encapsulation of Fe3O4 for Increased Reversibility in Li+ Storage by the Conversion Reaction. *J. Mater. Chem.* **2012**, *22*, 7845–7850.
61. Ding, F.; Xu, W.; Choi, D.; Wang, W.; Li, X.; Engelhard, M. H.; Chen, X.; Yang, Z.; Zhang, J.-G. Enhanced Performance of Graphite Anode Materials by AlF3 Coating for Lithium-Ion Batteries. *J. Mater. Chem.* **2012**, *22*, 12745–12751.
62. Xu, W.; Chen, X.; Wang, W.; Choi, D.; Ding, F.; Zheng, J.; Nie, Z.; Choi, Y. J.; Zhang, J.-G.; Yang, Z. G. Simply AlF3-Treated Li4Ti5O12 Composite Anode Materials for Stable and Ultrahigh Power Lithium-Ion Batteries. *J. Power Sources* **2013**, *236*, 169–174.